Dalton Transactions

ROYAL SOCIETY OF CHEMISTRY

PAPER

View Article Online
View Journal | View Issue

Cite this: *Dalton Trans.*, 2025, **54**, 14809

Distinct reactivity of iron dihydride *vs.* iron (hydride)(borohydride) bearing the same bulky PNP ligand in hydrogenation of alkenes and alkynes

Dilip K. Pandey, [a] Tatiana Gridneva, [a] Eugene Khaskin, [a] Robert R. Fayzullin, [b] Serhii Vasylevskyi [a] and Julia R. Khusnutdinova *[a]

Received 9th June 2025,
Accepted 29th August 2025

DOI: 10.1039/d5dt01350j

rsc.li/dalton

An iron dihydrido complex [(Me_4PNP^{iPr})$Fe(H)_2(N_2)$] with a bulky tetramethylated PNP pincer ligand, Me_4PNP^{iPr}, is an active catalyst for full hydrogenation of internal alkynes and alkenes, while its reactivity with terminal alkynes leads to its deactivation *via* bis-acetylide complex formation. Such reactivity is distinctly different from that of the previously reported hydrido-borohydrido complex [(Me_4PNP^{iPr})$FeH(\eta^2$-$BH_4)$], which showed selective semihydrogenation of terminal alkynes, but was unreactive toward alkenes and internal alkynes. This is also in contrast to the reactivity of the Fe^{II} dihydride analogue with a classical, CH_2-arm PNP pincer ligand, [(^{CH2}PNP)$Fe(H)_2(N_2)$], which showed low conversion with internal alkenes and quick degradation. A combined experimental and DFT study was employed to elucidate the differences in the selectivity of alkyne hydrogenation as a function of the complex structure and the ligand steric bulk, as well as the interplay between sterics and the relative preferences of the Fe^0 over Fe^{II} species as a function of steric congestion at the ligand.

Introduction

The development of new catalysts based on Earth-abundant and non-toxic metals such as iron as an alternative to precious metal-based catalysts for hydrogenation is an important goal toward sustainable and cost-efficient catalytic processes. Many examples of structurally diverse first-row transition metal hydrides have been reported as catalysts for hydrogenation of alkenes and alkynes, many of which are supported by strongly chelating, tridentate pincer ligands.[1–11] In this regard, iron is an ideal metal for catalysis, due to its low cost, comparatively low toxicity, and high abundance.[12–22]

The Chirik group reported the bis(imino)pyridine-ligated [(^{iPr}PDI)$Fe(N_2)_2$] complex (^{iPr}PDI = 2,6-(2,6-$^{i}Pr_2C_6H_3N$ = $CMe)_2C_5H_3N$), which forms an Fe^0 dihydrogen complex in solution in the presence of H_2, demonstrating catalytic activity with a broad substrate scope, including olefins with diverse functional groups and internal alkynes.[23] Later, the same group reported the dinitrogen *cis*-dihydride complex [(^{CH2}PNP^{iPr})$FeH_2(N_2)$], which promotes hydrogenation of 1-hexene under 4 bar of H_2 with a conversion of more than 98%, whereas only 10% of the cyclohexene was converted into hydrogenated cyclohexane. The lack of reactivity in hydrogenation of internal alkenes was attributed to the low stability of the complex.[24] Later, a different multidentate ligand, bis(arylimidazol-2-ylidene)pyridinyl, was introduced to produce [(^{R}CNC)$Fe(N_2)_2$] (R = Me, Mes) complexes, which were active catalysts for the hydrogenation of challenging trisubstituted and tetrasubstituted alkenes.[25] An acridine-derived pincer complex [(^{HACR}PNP)$Fe(CH_3CN)(\eta^2$-$CH_3CHCNBH_3)$], reported by the Milstein group, hydrogenates internal alkynes very efficiently at a high temperature of 90 °C.[26] Jones and co-workers reported the hydrogenation of styrene derivatives using the aliphatic pincer complex [(PN^HP^{iPr})$Fe(H)_2(CO)$] (PN^HP^{iPr} = NH(CH_2 $CH_2PiPr_2)_2$) as a catalyst; in this work, while various styrene derivatives were reduced with high conversion and selectivity, nonpolar aliphatic alkenes such as 1-hexene were unreactive even at increased temperature and pressure.[27] Subsequently, Gade and co-workers reported high-spin, bis(phosphino)carbazole [(PNP)Fe(alkyl)] pincer complexes that functioned as precatalysts for alkene hydrogenation: secondary aliphatic alkenes, such as 2-pentene and 2-hexene, were hydrogenated, while *E*-stilbene gave only 34% conversion after 3 days.[28] The Turculet group reported a [(PSiP)$Fe^{II}(H)(N_2)_2$] precatalyst for the hydrogenation of a variety of alkenes at a higher H_2 pressure of 10 bar at 65 °C.[29] Finally, Kirchner and co-workers developed (^{NMe}PNP)Fe hydride cationic pincer com-

[a]*Okinawa Institute of Science and Technology Graduate University, 1919-1 Tancha, Onna-son, Okinawa, 904-0495 Japan. E-mail: juliak@oist.jp*
[b]*Arbuzov Institute of Organic and Physical Chemistry, FRC Kazan Scientific Center, Russian Academy of Sciences, 8 Arbuzov Street, Kazan, 420088, Russian Federation*

plexes supported by an N–Me arm that catalyze the semihydrogenation of internal alkynes.[30]

Overall, previous work in the area by a number of groups outlined above shows that modification of the pincer ligand framework can be used as a strategy to achieve the desired level of activity and selectivity. The caveat is that preparation of a different ligand scaffold is required to achieve hydrogenation of various substrates such as cyclic, acyclic (internal and terminal) alkenes, terminal alkynes, and internal alkynes. From a practical point of view however, the ability to maintain the same pincer ligand framework while modulating the iron hydride activity by more convenient methods, such as choosing different hydride sources during complex synthesis or pre-catalyst activation, would provide a more convenient synthetic approach to achieve the desired catalytic reactivity without elaborate ligand modifications. Moreover, if significant changes in the activity and selectivity are achieved, it would provide important insight into reactivity control in iron hydride catalysis.

In this work, we demonstrate that the reactivity and selectivity of iron hydrides obtained from the same iron dibromide precursor supported by the bulky Me_4PNP^{iPr} ligand can be controlled by the choice of the hydride source (Fig. 1). Significantly enhanced reactivity is obtained, leading to full hydrogenation of internal alkynes and hydrogenation of terminal and internal alkenes, when using the neutral [$(Me_4PNP^{iPr})Fe(H)_2(N_2)$] complex obtained from iron dibromide and $NaHBEt_3$ or $LiHBEt_3$. This can be contrasted to a previously reported hydride complex with the same ligand, [$(Me_4PNP^{iPr})Fe(H)(\eta^2\text{-}BH_4)$], obtained by treatment of iron dibromide with $NaBH_4$, which was selective toward terminal alkyne semihydrogenation only, and was inactive towards alkenes and internal alkynes. The presence of a sterically congested pincer ligand in [$(Me_4PNP^{iPr})Fe(H)_2(N_2)$] plays a role, as the analogous non-bulky analogue containing a classical, non-methylated CH_2-arm ^{CH2}PNP ligand showed limited stability and a lack of reactivity with internal alkenes. Therefore, both steric bulk and the hydride source serve as convenient tools to control catalyst selectivity and reactivity within the same family of structurally similar Fe complexes.

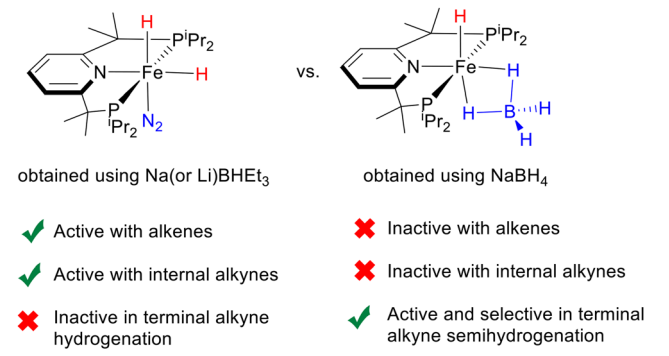

Fig. 1 Comparison of the reactivity of $(Me_4PNP^{iPr})Fe$ hydride complexes in catalytic hydrogenation of alkenes and alkynes at room temperature.

Results and discussion

Synthesis of iron dibromide, dihydride, and dicarbonyl complexes

[$(^{Me_4}PNP^{iPr})FeBr_2$] complex **1** was obtained in 93% yield by stirring equivalent amounts of a tetramethylated PNP pincer ligand, Me_4PNP^{iPr}, and anhydrous $FeBr_2$ at room temperature (RT) overnight (Scheme 1). A similar synthetic procedure has been previously used to prepare other iron(II) dihalide complexes with pincer ligands.[31,32] Paramagnetic complex **1** was characterized by UV-vis, FT-IR spectroscopy, and single-crystal X-ray diffraction (SC-XRD). Complex **1** shows a distorted pentacoordinate geometry with P1–Fe1–P2, N1–Fe1–Br1, and N1–Fe1–Br2 angles of 152.78(3)°, 127.45(5)°, and 123.31(5)°, respectively. The geometry index (τ_5) of complex **1** is 0.42, indicative of a geometrical intermediate between square pyramidal (with $\tau_5 = 0$ expected for an ideal square pyramidal structure) and a trigonal bipyramidal structure (with $\tau_5 = 1$ expected for an ideal trigonal bipyramidal structure). The Fe–N distance is 2.278(2) Å, and the Fe–P distances are 2.4859(7) and 2.4755(7) Å. The magnetic moment of complex **1** was measured by the Evans method in solution at RT, giving a μ_{eff} value of $4.9\mu_B$ in CD_2Cl_2 solution, reflecting four unpaired d-electrons in a high-spin complex. Treatment of complex **1** with 2.2 equiv. of $NaBHEt_3$ or $LiBHEt_3$ under an atmosphere of dinitrogen resulted in a diamagnetic, violet solution that contained complex **2** [$(Me_4PNP^{iPr})FeH_2(N_2)$] (Scheme 1), which was identified by NMR spectroscopy. Cooling the pentane solution of **2** to −35 °C produced single crystals suitable for SC-XRD that confirmed the presence of a coordinated dinitrogen ligand, along with two hydride ligands (Fig. 2).

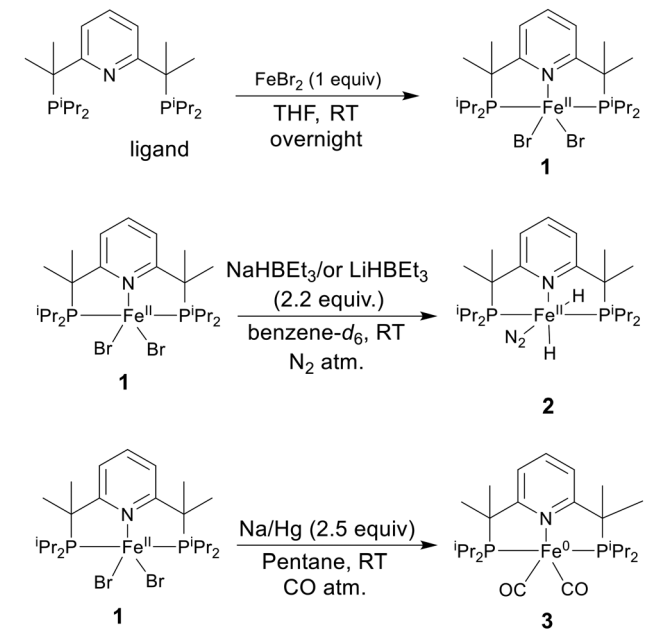

Scheme 1 Synthesis of iron complexes with the $Me_4PNP^{i}Pr$ ligand.

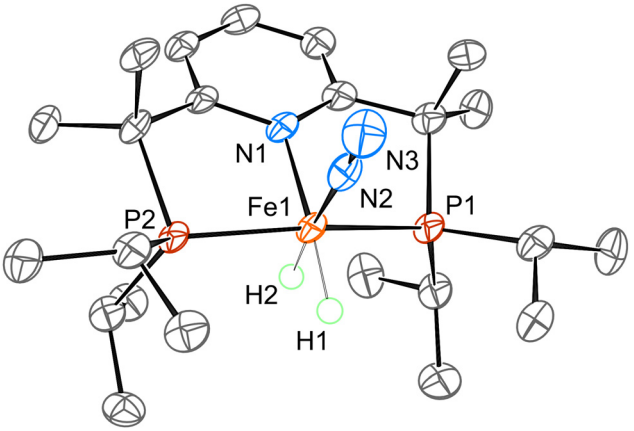

Fig. 2 Structure of complex **2** with thermal ellipsoids at the 70% probability level for nonhydrogen atoms. Hydrogen atoms except for [Fe–]H1 and [Fe–]H2 are omitted for clarity. Selected internuclear distances [Å] and valence angles [°]: Fe1–P1 2.1521(6), Fe1–P2 2.1458(7), Fe1–N1 2.004(2), Fe1–N2 1.794(2), Fe1–H1 1.547(10), Fe1–H2 1.520(10), P1–Fe1–P2 162.12(3), N1–Fe1–P1 86.15(6), N1–Fe1–P2 86.70(6), N1–Fe1–H1 168.7(15), N1–Fe1–H2 90.1(14), N1–Fe1–N2 99.57(9), H1–Fe1–H2 79(2), and H1–Fe1–N2 91.7(15).

Due to the product's limited stability, characterization was performed *in situ* just after mixing complex **1** with $NaBHEt_3$ or $LiBHEt_3$ in benzene-d_6. An almost complete conversion of iron dibromide complex **1** to complex **2**, [$(Me_4PNP)FeH_2(N_2)$], in the presence of either $NaBHEt_3$ or $LiBHEt_3$, was established by integration against mesitylene as an internal standard. The ^1H NMR spectrum exhibited diagnostic resonances for the two inequivalent hydrides that appear as two triplets of doublets centered at −18.30 (J_{H-H} = 21 Hz, J_{P-H} = 45 Hz) and −11.8 ppm (J_{H-H} = 21 Hz, J_{P-H} = 57 Hz). The appearance of two inequivalent iron hydrides in the NMR spectrum suggests that the solution structure is analogous to the X-ray structure (Fig. 1) where they are present in mutually *cis*-positions, with another coordination site occupied by dinitrogen. The $^{31}P\{^1H\}$ spectrum exhibits a resonance at 123.7 ppm. Dinitrogen coordination to complex **2** was also confirmed through infrared spectroscopy, which exhibited an N≡N stretch at 2007 cm^{-1}. This frequency is lower than the N_2 stretch at 2016 cm^{-1} reported for Chirik's complex [$(^{CH2}PNP^{iPr})FeH_2(N_2)$] suggesting the presence of a more electron-rich Fe center in arm-methylated **2**.[24]

We further attempted to obtain a stable Fe^0-dicarbonyl complex by treatment of complex **1** with 20% sodium amalgam in pentane under a carbon monoxide atmosphere, similar to the synthetic approach reported for the CH_2-arm $^{CH2}PNP^{iPr}$ ligand by Chirik and co-workers, which produced a blue color solution after 12 h.[24] Filtration followed by evaporation of pentane provided a brownish-red solid (complex **3**), whose structure was confirmed by NMR, IR, UV spectroscopy, and single-crystal X-ray diffraction. The CO peak is observed at 222 ppm in the $^{13}C\{^1H\}$ NMR spectrum. The SC-XRD structure of complex **3** features P1–Fe1–P2, N1–Fe1–C1, N1–Fe1–C2, and C1–Fe–C2 angles of 164.971(18)°, 120.17(6)°, 119.81(6)°, and 120.02(7)°, respectively, where two carbonyls and a pyridine nitrogen form an equatorial plane, and two phosphorus donors are axial, with a slight bend towards the pyridine ring (Fig. 3). The C–O bond distances in the carbonyls are 1.180(2) Å and 1.178(2) Å, longer than the carbonyl C–O bond distances in the analogous CH_2-arm [$(^{CH2}PNP^{iPr})Fe(CO)_2$] complex reported by Chirik and co-workers (1.1734(11) Å). The Fe–C bond distances in **3** are 1.7417(15) Å and 1.7438(16) Å, slightly longer than those reported in [$(^{CH2}PNP^{iPr})Fe(CO)_2$] (1.7325(9) Å), but still within the range reported for Fe(0) dicarbonyl complexes supported by PNP pincer ligands.[33–35]

The geometry index (τ_5) of complex **3** is 0.75, exhibiting a preference for the distorted trigonal bipyramidal structure. The Fe–N distance is 2.0575(12) Å, and the Fe–P distances are both equal to 2.1873(4) Å, which are only slightly shorter as compared to a previously reported [$(^{CH2}PNP)Fe(CO)_2$] complex.[24] Two intense carbonyl bands were observed in the solid-state infrared spectrum at 1835 and 1774 cm^{-1}, as expected for *cis*-dicarbonyl complexes. The CO stretching vibrations in **3** are present at lower frequencies compared to the nearly trigonal bipyramidal dicarbonyl complexes with a CH_2-arm [$(^{CH2}PNP^{iPr})Fe(CO)_2$] (1842 and 1794 cm^{-1})[24] and Kirchner's NH-arm and NMe-arm analogues [$(^{NH}PNP^{iPr})Fe(CO)_2$] (1866 and 1816 cm^{-1}) [$(^{NMe}PNP^{iPr})Fe(CO)_2$] (1856 and 1802 cm^{-1}) which exhibited CO stretches at even higher frequencies.[33,36] This reflects the more electron-rich character of the Fe center that engages in stronger π-backdonation to CO. The series of complexes arranged by back-donation can be ranked as follows: Me_4PNP^{iPr} > $^{CH2}PNP^{iPr}$ > $^{NMe}PNP^{iPr}$ > $^{NH}PNP^{iPr}$, consistent with the Me_4PNP^{iPr} ligand being the strongest electron donor. Compared to other PNP-donor pincer motifs, the CO stretching frequencies in **3** are similar to those reported for square pyramidal and trigonal bipyramidal Fe(0) dicarbonyl complexes with aliphatic PN^HP ligands (in the range of 1884–1760 cm^{-1});[34,35,37] however, they are higher

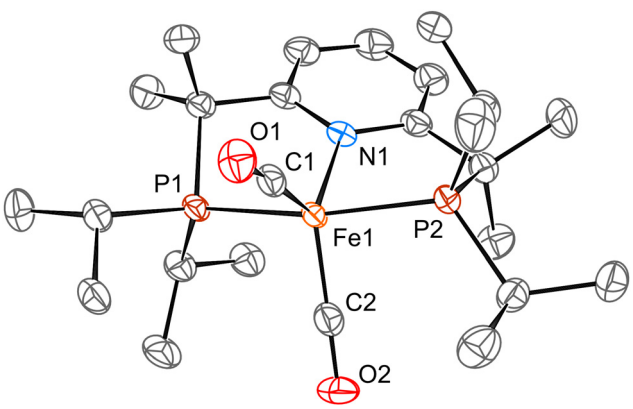

Fig. 3 Structure of complex **3** with thermal ellipsoids at the 70% probability level for nonhydrogen atoms. Hydrogen atoms are omitted for clarity. Selected interatomic distances [Å] and valence angles [°]: Fe1–P1 2.1873(4), Fe1–P2 2.1873(4), Fe1–N1 2.0575(12), Fe1–C1 1.7417(15), Fe1–C2 1.7438(16), P1–Fe1–P2 164.971(18), N1–Fe1–P1 82.23(4), N1–Fe1–P2 82.75(4), N1–Fe1–C1 120.17(6), N1–Fe1–C2 119.81(6), and C1–Fe1–C2 120.02(7).

when compared to a dicarbonyl with an anionic pyrrole-based PNP ligand (1787 and 1731 cm^{-1}).[38]

Catalytic reactivity in hydrogenation

To study the reactivity of complex **1** in hydrogenation and optimize its catalytic activity, we used styrene as a model substrate under 1 bar of H_2 (1 bar) in anhydrous THF solvent at room temperature. The paramagnetic iron(II)dibromide complex **1** and the dicarbonyl complex **3**, [$(Me_4PNP)Fe^0(CO)_2$], did not produce detectable amounts of hydrogenated products (Table 1, entries 1 and 2). We used freshly prepared complex **2** (obtained by mixing complex **1** and $LiHBEt_3$ immediately before the catalytic trial) during the optimization. The *in situ* prepared complex **2** was found to be very effective, with almost complete conversion of styrene, giving a 99% yield of ethylbenzene after 1 hour of reaction time in THF under 1 bar of H_2 pressure (Table 1, entries 3 and 4). Using $FeBr_2$ with $LiHBEt_3$ but without the Me_4PNP ligand was not efficient, providing only 40% of hydrogenated ethylbenzene after 4 h (Table 1, entry 5). Different hydride sources such as $NaHBEt_3$, $NaBH_4$, $LiAlH_4$, and $LiBH_4$ were also screened during optimization of the catalytic reactivity of *in situ* generated **2**. $NaHBEt_3$ showed comparable efficiency to $LiHBEt_3$ and afforded ethylbenzene with 99% yield in 1.5 h (Table 1, entry 6). $NaBH_4$ and $LiBH_4$ were ineffective and did not provide the hydrogenated product, while using $LiAlH_4$ gave only 10% of ethylbenzene (Table 1, entries 7–9). This result is not surprising considering that BH_4^- is not a good hydride transfer agent.[39] Changing the reaction solvent to benzene increased the reaction time to 1.5 h and 4 h with $LiHBEt_3$ and $NaHBEt_3$ additives, respectively, giving 99% of the hydrogenated product (Table 1, entries 10 and 11).

The optimized conditions for styrene hydrogenation using the *in situ* prepared catalyst [$(Me_4PNPiPr)FeH_2(N)_2$] were then used to further explore the substrate scope and reactivity limitations (Scheme 2). Substrates such as styrene, *para*-methoxystyrene, *para*-fluorostyrene, and *para*-phenylstyrene gave hydrogenated products with a 99% yield at 1 bar H_2 pressure within 1–2 h (Scheme 2, **A1**–**A3**, **A5**). *para*-Chlorostyrene gave 90% of the hydrogenated product at 1 bar of H_2 (Scheme 2, **A4**). A more electron-poor substrate, pentafluorostyrene, gave only 45% yield (Scheme 2, **A6**). An aliphatic terminal alkene, 1-octene, was nearly fully hydrogenated to octane (Scheme 2, **A7**). When 1-octene was used under the same conditions but without hydrogen gas, a mixture of internal octenes formed according to NMR and GC-MS, suggesting repeated hydride insertion and elimination reactions in the absence of H_2.

The protocol was subsequently applied to internal acyclic alkenes. β-Methylstyrene afforded >99% of propylbenzene after 16 h (Scheme 2, **A8**). The hydrogenation of *Z*-stilbene required 24 hours and 5 bar of H_2, and led to only 52% of diphenylethane, with the remaining product being (*E*)-stilbene (Scheme 2, **A9**). Cyclooctene yielded 80% of cyclooctane, while 1,5-cyclooctadiene produced 47% monohydrogenated cyclooc-

Table 1 Initial optimization and comparison of pre-catalysts for styrene hydrogenation[a]

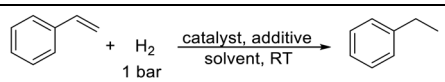

Entry	Catalyst (mol%)	Additive (mol%)	Solvent	Time (h)	Yield[b] (%)
1	**1** (5)	—	THF	24	n.d.
2	**3** (5)	—	THF	24	n.d.
3	**1** (5)	$LiHBEt_3$ (15)	THF	16	99
4	**1** (5)	$LiHBEt_3$ (15)	THF	1	99
5	$FeBr_2$ (5)	$LiHBEt_3$ (15)	THF	4	40
6	**1** (5)	$NaHBEt_3$ (15)	THF	1.5	99
7	**1** (5)	$NaBH_4$ (15)	THF	16	n.d.
8	**1** (5)	$LiBH_4$ (15)	THF	16	n.d.
9	**1** (5)	$LiAlH_4$ (15)	THF	16	10
10	**1** (5)	$LiHBEt_3$ (15)	C_6D_6	1.5	99
11	**1** (5)	$NaHBEt_3$ (15)	C_6D_6	4	99

[a] Typical conditions: styrene (0.1 mmol) and catalyst (0.005 mmol), additive (3.0 equiv. w.r.t. catalyst), solvent (0.5 mL), 1 bar of H_2. [b] NMR yields were determined by integration against mesitylene as an internal standard. n.d. – not detected.

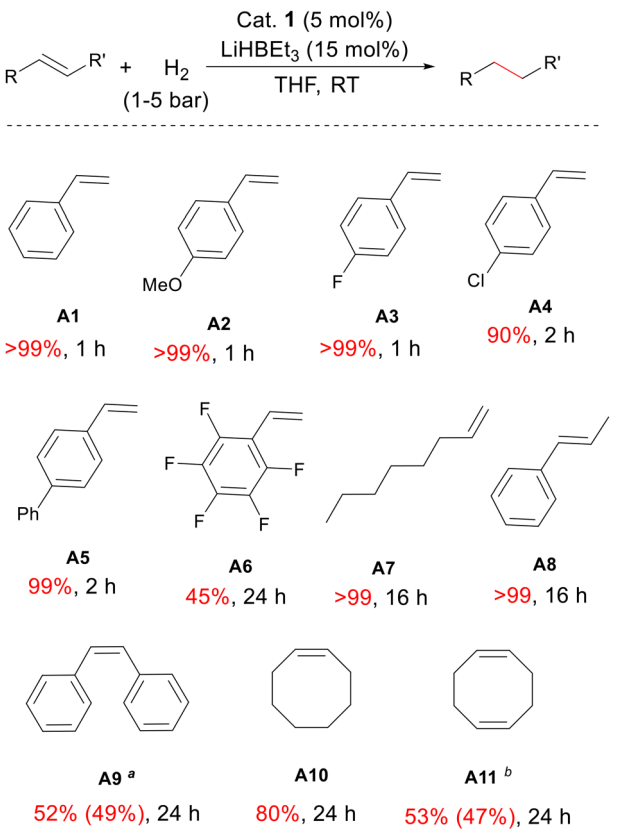

Scheme 2 Hydrogenation of alkenes catalyzed by *in situ* formed complex **2**. Typical conditions: alkene (0.1 mmol), H_2 (1–5 bar), cat. **1** (5.0 mol%), THF (0.5 mL), 23 °C. Yields were determined by ^1H NMR against mesitylene as an internal standard. [a] Yield in parenthesis is for isomerization of the starting material to (*E*)-stilbene. [b] Yield in parenthesis is for the product cyclooctene. **A1**–**A8** were hydrogenated under 1 bar H_2, and **A9**–**A11** were hydrogenated under 5 bar H_2.

tene and 53% dihydrogenated cyclooctane under 5 bar of H_2 after 24 h (Scheme 2, **A10**, **A11**).

We also assessed the catalytic activity of **2** in the hydrogenation of internal alkynes at 5 bar of H_2. 1,2-Diphenylacetylene produced 98% semihydrogenated stilbene (*E*/*Z* = 92/6) within 4 hours, with only 2% of the completely hydrogenated 1,2-diphenylethane product present (Scheme 3, **B1**). Continuing the reaction for 48 hours generated 52% of 1,2-diphenylethane and 48% of (*E*)-stilbene, while no *Z*-stilbene was detected. The hydrogenation of 1-phenyl-1-propyne provided 25% of semihydrogenated (*E*)-1-phenyl-1-propene and 68% of the completely hydrogenated product in 24 h at RT (Scheme 3, **B2**). Silylated internal alkynes resulted in moderate amounts of hydrogenated products and were not particularly selective substrates (Scheme 3, **B3–B6**). Substrates such as trimethyl(phenylethynyl)silane and trimethyl(naphthalen-2-ylethynyl)silane provided 47% (*E*/*Z* = 38/9) and 26% (*E*/*Z* = 24/2) of the semihydrogenated products, respectively, while 9% of the fully hydrogenated product was observed for trimethyl(phenylethynyl)silane after 24 hours (Scheme 3, **B3**, **B4**). Alkynes with heterocyclic aryl groups, such as trimethyl(pyridin-3-ylethynyl)silane, yielded only 5% of the hydrogenated *E*-isomer and 65% of the fully hydrogenated product, whereas trimethyl(furan-3-ylethynyl)silane afforded 35% of the semihydrogenated *Z*-isomer product, while the fully hydrogenated product was not observed (Scheme 3, **B5**, **B6**).

Interestingly, activity in hydrogenation of both terminal and internal alkenes and internal alkynes contrasts with the observations in our previous reports with the same PNP ligand. For example, the monohydride complex **4**, [(Me_4PNP^{iPr})$FeH(\eta^2\text{-}BH_4)$], was unreactive with styrene, which led to its successful application for the selective semihydrogenation of terminal alkynes. No hydrogenation was observed with internal alkynes such as 1,2-diphenylacetylene and 1-phenyl-1-propyne (Scheme 4).[40,41]

Chirik and co-workers have previously reported the synthesis and characterization of the classical CH_2-arm [($^{CH2}PNP^{iPr}$)$FeH_2(N_2)$] **5**, obtained by treatment of [($^{CH2}PNP^{iPr}$)$FeCl_2$] with $NaBHEt_3$, which showed low conversion in hydrogenation of cyclohexene after 6–24 h, while it was an active catalyst in hydrogenation of 1-hexene. The lack of activity in the case of **5** was attributed to its low stability and catalyst decomposition during the course of the reaction. To directly compare the reactivity of **2** and **5**, we evaluated their reactivity under analogous conditions using cyclooctene as a model substrate. Both the complexes were prepared *in situ* using $LiBHEt_3$

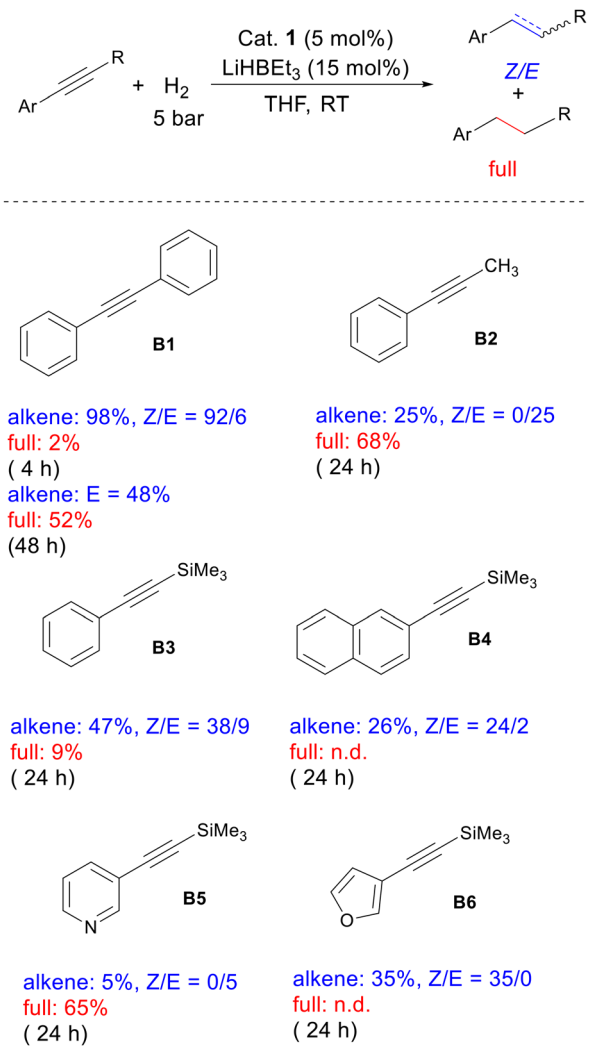

Scheme 3 Hydrogenation of internal alkynes catalyzed by *in situ* formed complex **2**. Typical conditions: (a) alkyne (0.1 mmol), H_2 (5 bar), cat. 1 (5.0 mol%), THF (0.5 mL), 23 °C, 4–24 h. Yields were determined by ^1H NMR against mesitylene as an internal standard.

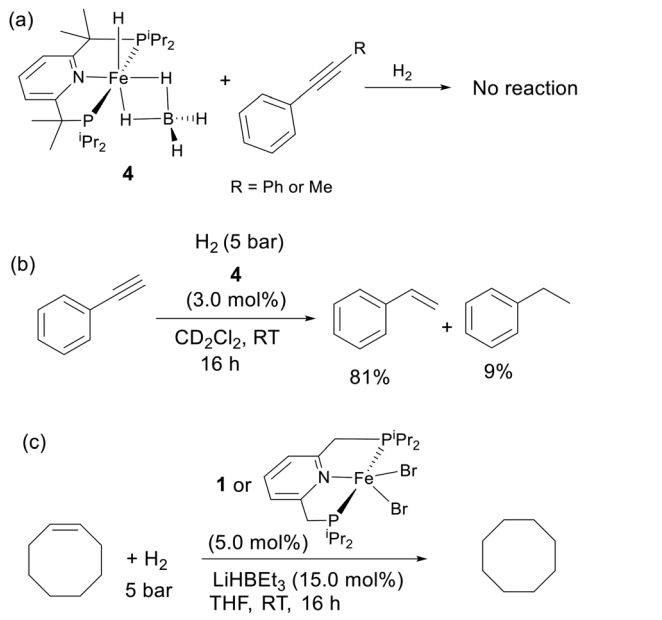

Scheme 4 Reactivity of previously reported complexes **4** and **5** in hydrogenation of alkenes and alkynes.

and the respective iron dibromide complexes (Scheme 4c). When *in situ* generated **2** was used as the catalyst for *cis*-cyclooctene hydrogenation, significant conversion (80%) was achieved after 24 h as compared to complex **5**, which led to 12% conversion under analogous conditions. Thus, one possible advantage of a tetramethylated ligand in **2** could be to provide a more stable, catalytically active complex which allows for continuous hydrogenation without catalyst degradation for extended periods of time when compared to **5**.

Considering that our previously reported monohydride complex **4** was selective for semihydrogenation of terminal alkynes, we then examined the reactivity of the dihydride nitrogen complex **2** in the analogous reaction. Surprisingly, the attempted hydrogenation of phenylacetylene using *in situ* generated **2** resulted in only 7% of styrene after 5 hours under 5 bar of H_2 in THF (Scheme 5). Further extending the reaction time to 24 resulted in the formation of 24% of styrene, 56% of phenylacetylene trimerization products (a mixture of two isomers, 1,2,4-triphenylbenzene and 1,3,5-triphenylbenzene), and 16% of unreacted phenylacetylene (Scheme 5), confirmed by NMR and GC-MS. When the filtered reaction mixture was kept at −35 °C for crystallization, a new complex, [(Me_4PNP)Fe bis(phenylacetylide)] **6**, was obtained and characterized by SC-XRD (Fig. 4). We assume that this is an inert, off-cycle species and its formation may explain the lack of activity in terminal alkyne semihydrogenation.

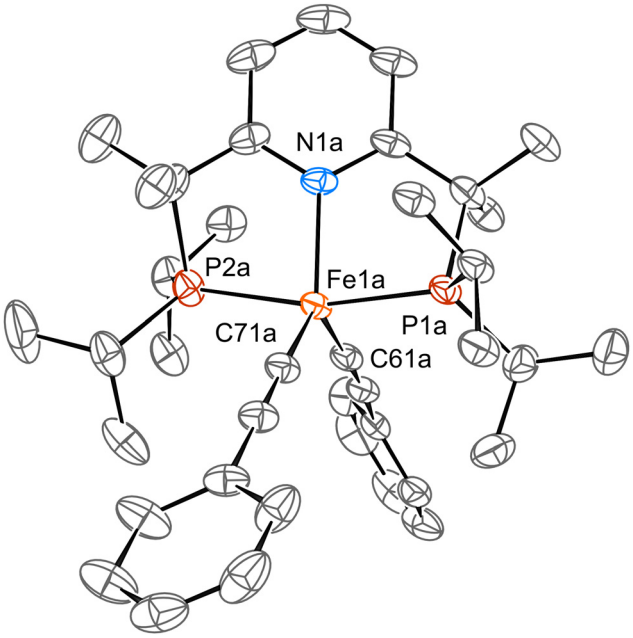

Fig. 4 Structure of complex **6** with thermal ellipsoids at the 40% probability level for nonhydrogen atoms. Hydrogen atoms are omitted for clarity. Selected interatomic distances [Å] and valence angles [°]: Fe1a–P1a 2.2127(6), Fe1a–P2a 2.2326(7), Fe1a–N1a 2.0719(17), Fe1a–C61a 1.963(2), Fe1a–C71a 1.959(2), P1a–Fe1a–P2a 165.53(3), and C61a–Fe1a–C71a 122.77(9).

Mechanistic investigation

To establish whether a radical hydrogenation mechanism could be operative under these conditions, a radical clock experiment was performed using (1-cyclopropylvinyl)benzene as a terminal alkene substrate, which resulted in the formation of non-ring-opened hydrogenation products exclusively in 40% and 72% yields under 1 bar and 5 bar of H_2, respectively. No ring-opened product was detected by NMR spectroscopy and GC-MS, arguing against a radical hydrogenation mechanism (Scheme 6).[42–44] A homogeneity mercury drop test was performed, which resulted in 99% yield of the ethylbenzene hydrogenation product with styrene under the standard reaction conditions. Using a substoichiometric amount of PPh_3 (25 equiv. to Fe) to establish if a catalytically active heterogeneous iron catalyst is formed did not result in significant suppression of the catalytic activity and produced 92% of the hydrogenated product using styrene under standard conditions.[45–47]

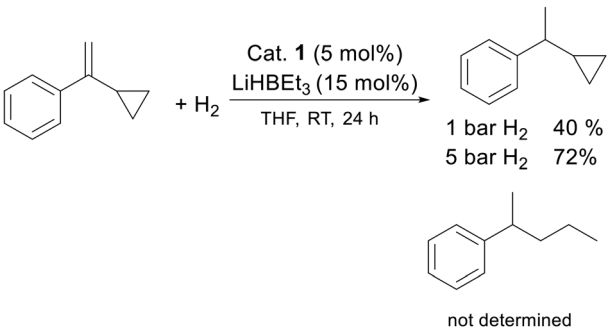

Scheme 6 Radical clock experiment.

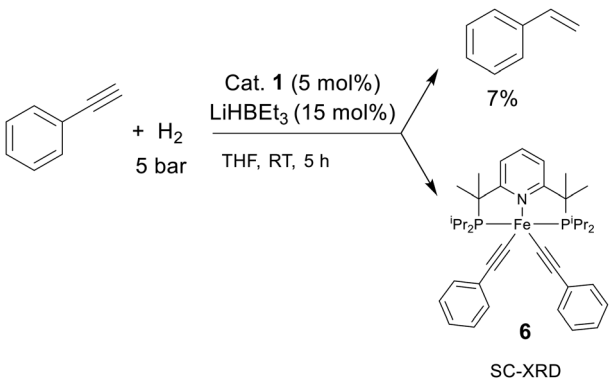

Scheme 5 Attempted terminal alkyne hydrogenation by complex **1**.

2D Exchange Spectroscopy (EXSY) NMR experiments at 23 °C established the presence of cross-peaks between the two hydride signals, indicative of an exchange process between the two hydrides. Similar behavior was observed in the [(^{CH2}PNP)$FeH_2(N_2)$] complex with a non-bulky CH_2-arm PNP ligand reported by Chirik and co-workers. Such an exchange could involve the formation of an iron(0) η^2-dihydrogen complex followed by quick η^2-H_2 rotation, or the formation of a fluxional five-coordinate Fe^{II} dihydride formed *via* N_2 dissociation and

rebinding, similar to the exchange mechanism proposed for [(^{CH2}PNP)FeH$_2$(N$_2$)].[24]

When *in situ* prepared **2** was exposed to 1 bar of D_2 for 1 hour in benzene-d_6 solution, both Fe–H peaks disappeared, and ^{2}H NMR analysis revealed two peaks of Fe–D at −12.04 and −18.45 ppm, analogous to the parent complex. H/D exchange could involve either the reductive elimination of H_2 to produce an Fe(0) intermediate, or it can alternatively occur through non-classical Fe^{II} polyhydride complexes, similar to the mechanism proposed by Kirchner and co-workers for Fe complexes with PNP ligands containing the N–Me arm.[48] Accordingly, our computational study allowed us to find a path for hydride/hydrogen exchange *via* Fe polyhydrides with low barriers of 2.0 and 2.5 kcal mol^{-1}, calculated respectively for the twisted and bent conformations of the Me$_4$PNP^{iPr} ligand in these complexes (Scheme 7). An alternative hydride exchange mechanism *via* Fe(0) was considered, but all attempts to optimize an Fe(0)(η^2-H$_2$) intermediate were unsuccessful and converged to Fe^{II} for both possible conformations.

DFT calculations were performed to gain further insight into the reaction mechanism. In particular, we aimed to elucidate the reasons for the high catalytic activity of **2** in internal alkyne hydrogenation, which leads to gradual semihydrogenation, followed eventually by full hydrogenation (see above), which contrasts with the lack of reactivity of monohydride complex **4** with internal alkynes and the same ligand and under the same reaction conditions. This study also suggested that the tetramethylated, bulky Me$_4$PNP ligand imposes different structural preferences that are reflected in the stability of some Fe(0) *vs.* Fe(II) intermediates as compared to the classical CH$_2$-arm PNP ligand.

Calculations were performed using the M06-L functional[49] and def2-tzvp basis sets[50] for all elements as implemented in the Gaussian 16 package;[51] all structures were fully optimized in THF using the SMD model.[52] This method, used in our previous work,[40] showed good agreement of calculated and experimentally determined bond lengths (Table S1) and has demonstrated good performance for transition-metal complexes.[53] We first calculated the reaction profile for the full hydrogenation of 1,2-diphenylacetylene catalyzed by complex **2**.

Although we have considered possible outer-sphere pathways that would not involve N_2 dissociation, no accessible transition states could be identified. Therefore, we hypothesized that the reaction is initiated by dissociation of the dinitrogen ligand to give intermediate complex **Int1**, and coordination of diphenylacetylene (DPA) to give the intermediate DPA-coordinated complex **Int2a** which is endergonic by 17.2 kcal mol^{-1}. Interestingly, **Int2a** is not the most stable isomeric form, and it features a low-energy transition state (TS) for reductive H–H coupling to form **Int2b**, which is slightly more stable than **Int2a** by 0.9 kcal mol^{-1}. Based on the H–H distance and structural parameters, **Int2b** can be described as an Fe^0 complex with an η^2-coordinated dihydrogen ligand (Scheme 8).

To examine whether the preference for the Fe^0 form is caused by the presence of a more sterically congested Me$_4$PNP^{iPr} ligand, we compared the relative stabilities of structural analogues of these isomers with the classical CH$_2$-arm ^{CH2}PNP^{iPr} ligand, **Int2a-CH$_2$** and **Int2b-CH$_2$**. However, in this case, the opposite trend was observed, with the Fe^{II} form **Int2a-CH$_2$** being more stable than the H$_2$-coupled Fe^0 form **Int2b-CH$_2$**, by 2.7 kcal mol^{-1}. The propensity of the Me$_4$PNP^{iPr} ligand to favor the **Int2b** form may be attributed to significant steric congestion between the Me and i-Pr substituents and coordinated DPA, which pushes DPA away from the ligand, disfavoring a six-coordinate, octahedral environment at Fe^{II}, while a nearly trigonal bipyramidal coordination at **Int2b** provides steric relief from the repulsion caused by the Me and i-Pr groups. The electronic differences at the Fe center exerted by methylated Me$_4$PNP^{iPr} compared to CH$_2$-arm PNP likely play a

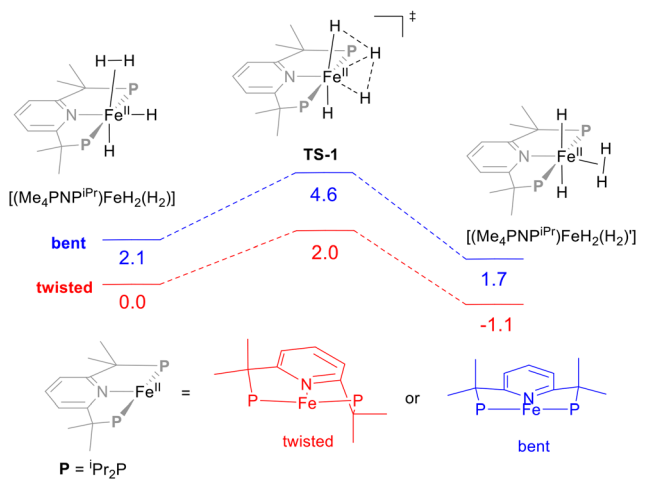

Scheme 7 Free energy profile for hydride/hydrogen exchange calculated for complexes containing PNP in two conformations: twisted (shown in red, with *C*Me$_2$ carbons on opposite sides of the PNP(Fe) coordination plane) and bent (shown in blue, with two *C*Me$_2$ carbons on the same side of the PNP(Fe) coordination plane).

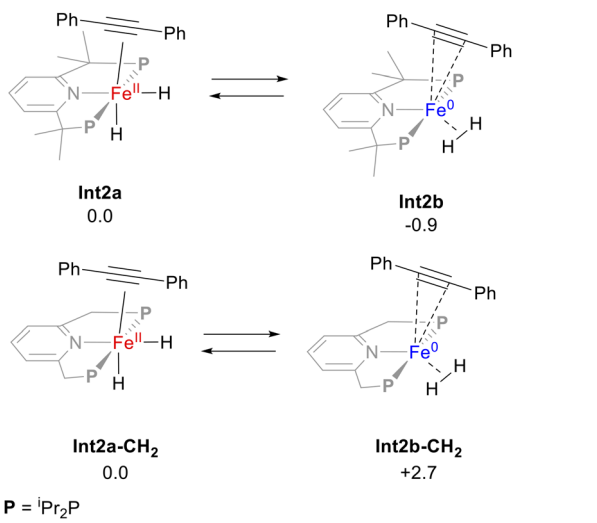

Scheme 8 Comparison of the free energies between the dihydride complexes and dihydrogen complexes (in kcal mol^{-1}).

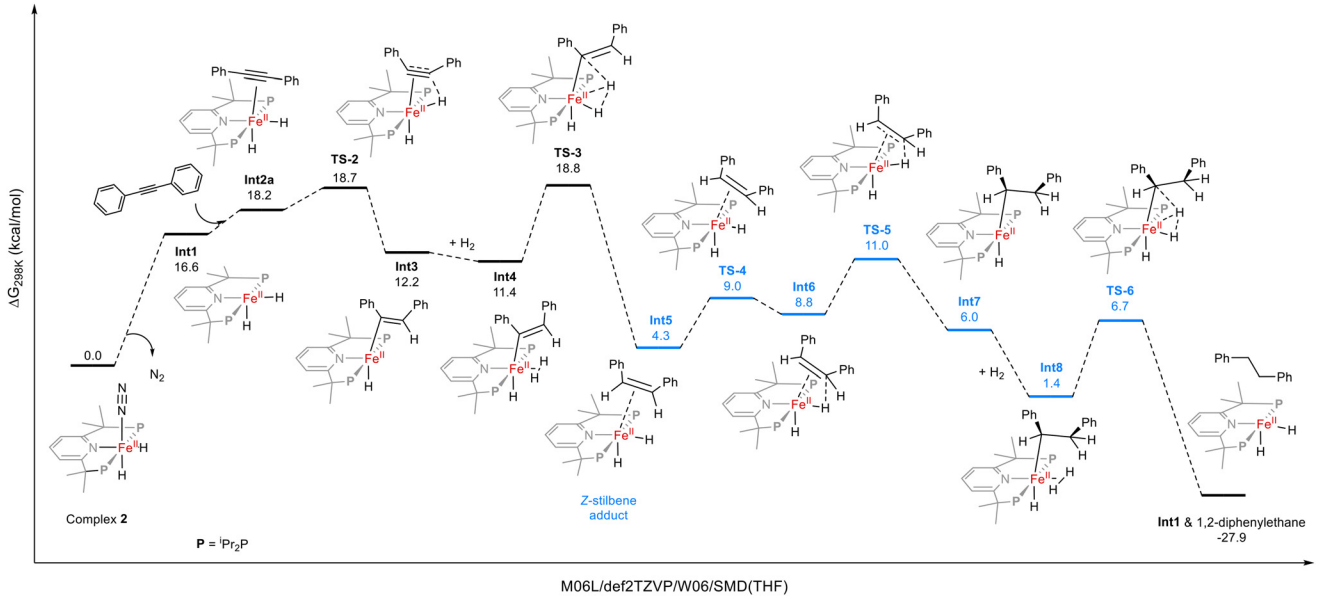

Scheme 9 Gibbs free energy profile for the complete hydrogenation of diphenylacetylene catalyzed by **2**.

much less important role in determining relative stabilities as the C≡C bond in coordinated DPA is only slightly elongated in the DFT-optimized **Int2b** (1.307 Å) compared to **Int2b-CH$_2$** (1.304 Å), suggesting that the contribution of π-backdonation to the coordinated alkyne is comparable. This indicates that manipulation of the sterics above the plane of PNP pincer ligands (*e.g.* through Me groups on the arms) can potentially be used as a tool to tune not only catalytic activity, but also to significantly change the energy of iron intermediates in different oxidation states.

While **Int2b** did not allow us to identify a direct pathway to the products, **Int2a** can undergo a low-barrier insertion to give **Int3**, which then coordinates another equivalent of H_2, followed by C–H coupling through **TS-3** to give a *Z*-stilbene adduct **Int5**, with a barrier of 18.8 kcal mol^{-1}. Following a similar mechanism, a second insertion to *Z*-stilbene and C–H coupling lead to the fully hydrogenated product 1,2-diphenylethane. The barriers for the second reaction where *Z*-stilbene is hydrogenated to diphenylethane are lower than those for the hydrogenation of the alkyne (highest at 11.0 kcal mol^{-1}), consistent with the observation that the reaction does not stop at *Z*-stilbene and continues to full hydrogenation.

We also considered the isomerization from the *Z*-adduct to the *E*-adduct, which may occur by the rotation of the C–C bond in **Int7**. A transition state **TS-7** that featured such a C–C bond rotation could be identified, leading to **Int9** which is an analogue of **Int7** with the phenyl groups pointing in opposite directions (Scheme 10). The low barrier of **TS-7** of +3.3 kcal mol^{-1} relative to **Int7** suggests that the rotation can easily proceed to form **Int9**, which can further undergo β-hydride elimination to form an *E*-stilbene adduct and release *E*-stilbene (Scheme 10).

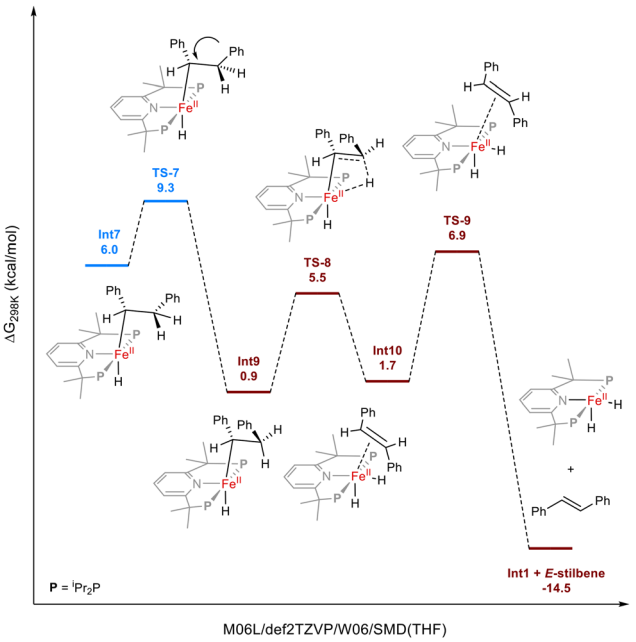

Scheme 10 Rotation of the C–C bond of **Int7** to form **Int9** and the release of *E*-stilbene (Gibbs free energies relative to complex **1** + DPA + 2H$_2$, Scheme 9).

Alternatively, **Int9** may undergo H_2 insertion followed by the final C–H coupling through **TS-10** to give the fully hydrogenated product (Scheme 11). The slightly higher barrier for *E*-stilbene hydrogenation (7.5 kcal mol^{-1}) for **TS-10** compared to 6.7 kcal mol^{-1} for **TS-6** is consistent with accumulation of *E*-stilbene during the course of the reaction.

To gain insight into the differences in the reactivities of **2**, which was active in hydrogenation of internal alkynes and

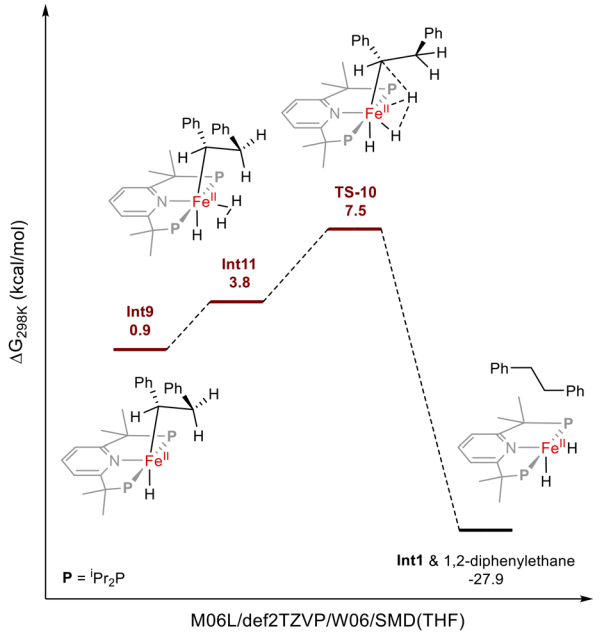

Scheme 11 Hydrogenation of the *E*-conformer **Int9** to form 1,2-diphenylethane (Gibbs free energies relative to complex **1** + DPA + $2H_2$, Scheme 9).

alkenes, and monohydride complex **4**, which was unreactive with these substrates,[40] we then calculated the first stage of internal alkyne hydrogenation using monohydride **4** as a pre-catalyst (Scheme 12). The free energies were calculated using an SMD solvation model in THF for direct comparison with complex **2**. This mechanism parallels the one reported in Kirchner's work[30] and our previous work.[40]

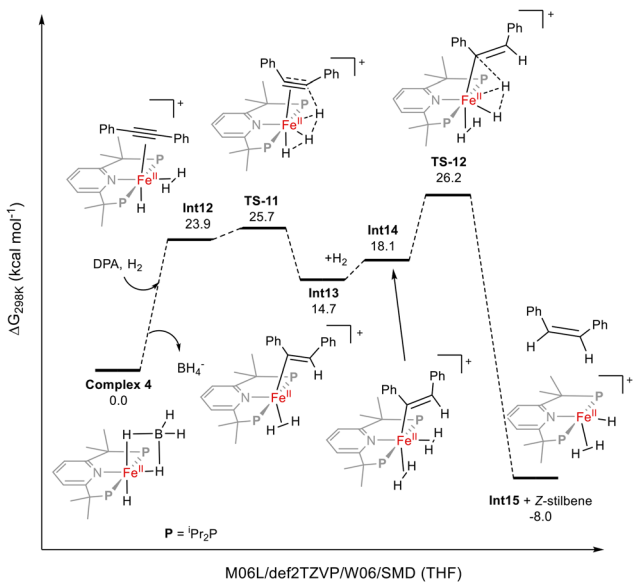

Scheme 12 Gibbs free energy profile for the semihydrogenation of diphenylacetylene catalyzed by **4**.

The first insertion step was characterized by a larger barrier in the case of complex **4** as compared to **2**, which could be due to the different nature of this step: while insertion in **2** occurs from an Fe–H fragment, in complex **4**, the transition state **TS-11** involves the transfer of an H-atom from the coordinated H_2 molecule and it must be accompanied by H–H bond splitting.

An even higher barrier of 26.2 kcal mol^{-1} is identified for the C–H coupling step in complex **4** *via* **TS-12**, which is 7.4 kcal mol^{-1} greater than for complex **2**, consistent with the contrasting reactivity of complexes **2** and **4** towards internal alkynes. This difference could be attributed to the more sterically congested nature of bis(hydrogen) intermediate **Int14**, formed by slightly thermodynamically unfavorable coordination of the second H_2 moiety to the initial product of insertion, **Int13**. For comparison, coordination of another molecule of H_2 is slightly favorable for **Int3**, the initial product of insertion starting from complex **2**.

Another possible factor contributing to the lack of reactivity of **4** with internal alkynes and alkenes could be the presence of BH_4^- as a competitive ligand for the vacant coordination site at iron, which allows only the least bulky substrate, a terminal alkyne, to successfully compete for Fe, while the N_2 ligand served as a good leaving group in the case of **2**.

The C–H coupling step barrier in the case of complex **4** is also significantly higher than the highest barrier calculated for phenylacetylene hydrogenation using **4** that was reported in our earlier publication,[40] explaining the high selectivity of this complex towards terminal triple bonds as opposed to internal triple bonds. The important difference when comparing the energy profiles for the hydrogenation of DPA (either with complex **2** or **4**) and hydrogenation of phenylacetylene with complex **2** is that in the case of DPA, the highest barrier is an alkene-forming C–H coupling step. In contrast, in the case of phenylacetylene and complex **4**, the highest barrier step was the first insertion to form a metal-bonded vinyl intermediate. This is mainly due to a significantly higher free energy for the 1,2-diphenylvinyl intermediates such as **Int4** or **Int14**, as compared to the analogous 2-phenylvinyl intermediates formed from the terminal alkyne phenylacetylene.[40] The destabilization of these 1,2-diphenylvinyl intermediates is attributed to the significant steric repulsion between the Me and i-Pr groups of the ligand and an Fe-bound phenyl-substituted vinylic carbon in a rigid 1,2-diphenylvinyl ligand.

Overall, the DFT calculations showed that the significantly higher reactivity of a dihydride precatalyst **2** compared to monohydride **4** towards internal alkynes is consistent with significantly lower barriers for the C–H coupling step in the formation of the internal alkene adduct. The enhanced reactivity of **4** towards terminal alkynes contrasts with its lack of reactivity with internal alkynes, which is likely due to significantly destabilized vinyl intermediates which experience significant steric repulsion between the rigid 1,2-substituted vinyl ligand with the bulky Me and i-Pr substituents of the modified pincer ligand.

Conclusions

In summary, different catalytic activities were observed with the same pre-catalyst, dibromide complex **1**, using two different hydride sources: $NaBH_4$, which as reported earlier, gives rise to a monohydride species **4**, and Li or $NaBEt_3H$, which produced a dihydride nitrogen complex **2**. Despite the similarity of complex **2** to the reported analogue with the classical and poorly catalytically active CH_2-arm PNP pincer, we obtained sustained catalytic activity in mild hydrogenation of terminal and internal alkenes as well as internal alkynes at room temperature and low H_2 pressure (1–5 bar). This shows that simple synthetic variations and the choice of the hydride source can result in contrasting reactivity, as the previously reported **4** allowed for the selective semihydrogenation of terminal alkynes, but was unreactive with alkenes and internal alkynes.

The computational study suggests that the presence of a bulky, tetramethylated Me_4PNP^{iPr} ligand alters the energy differences between Fe^{II} and Fe^0 redox states in the proposed dihydride/hydrogen intermediates with coordinated internal alkyne, favoring Fe^0 formation over Fe^{II}, *via* H–H coupling driven by steric repulsion caused by the Me and i-Pr groups of the bulky ligand.

A DFT analysis of the reaction profile provided the rationale for the higher reactivity of **2** towards internal alkynes, consistent with a significantly lower overall barrier for internal alkyne hydrogenation, with the highest barrier determined by the C–H coupling step of the vinyl intermediate.

While the lack of reactivity of **2** with terminal alkynes was not addressed through DFT studies, experiments confirm deactivation of the dihydride catalyst due to the formation of a paramagnetic bis-acetylide complex, which presumably does not engage in further reactivity with H_2, but may eventually lead to the observed, undesired alkyne trimerization, which was successfully suppressed with monohydride **4**.

Author contributions

D. K. P. performed synthesis, characterization and catalytic experiments. T. G. performed DFT calculations. E. K. designed the ligand and performed XRD measurements. R. R. F. and S. V. analyzed XRD data and refined the structures. The manuscript was written through contributions of all authors. All authors have given approval to the final version of the manuscript.

Conflicts of interest

There are no conflicts to declare.

Data availability

The data supporting this article have been included as part of the SI.

Supplementary information: synthesis and characterization details, Cartesian coordinates of optimized structures, animation and movies for transition states and IRC calculations. See DOI: **https://doi.org/10.1039/d5dt01350j**.

CCDC 2447918 (**1**), 2447919 (**2**), 2447920 (**3**), and 2447921 (**6**) contain the supplementary crystallographic data for this paper.[54a–d]

Acknowledgements

We thank the OIST Instrumental Analysis Section and Engineering Section for technical support and HPC for access to computational resources. R. R. F. performed crystal structure determination within the assignment for the Kazan Scientific Center of RAS. The authors acknowledge the Okinawa Institute of Science and Technology for funding. We thank Dr Shrinwantu Pal (Brandon University, Canada) for helpful discussions regarding DFT.

References

1 T.-P. Lin and J. C. Peters, *J. Am. Chem. Soc.*, 2014, **136**, 13672–13683.
2 P. J. Chirik, *Acc. Chem. Res.*, 2015, **48**, 1687–1695.
3 N. Gorgas and K. Kirchner, *Acc. Chem. Res.*, 2018, **51**, 1558–1569.
4 F. Kallmeier and R. Kempe, *Angew. Chem., Int. Ed.*, 2018, **57**, 46–60.
5 A. Mukherjee and D. Milstein, *ACS Catal.*, 2018, **8**, 11435–11469.
6 T. Zell and R. Langer, *ChemCatChem*, 2018, **10**, 1930–1940.
7 L. Alig, M. Fritz and S. Schneider, *Chem. Rev.*, 2019, **119**, 2681–2751.
8 B. L. Ramirez and C. C. Lu, *J. Am. Chem. Soc.*, 2020, **142**, 5396–5407.
9 A. Kumar, P. Daw and D. Milstein, *Chem. Rev.*, 2022, **122**, 385–441.
10 N. F. Both, A. Spannenberg, K. Junge and M. Beller, *Organometallics*, 2022, **41**, 1797–1805.
11 J. C. Ott, D. Bürgy, H. Guan and L. H. Gade, *Acc. Chem. Res.*, 2022, **55**, 857–868.
12 C. Bianchini, A. Meli, M. Peruzzini, F. Vizza, F. Zanobini and P. Frediani, *Organometallics*, 1989, **8**, 2080–2082.
13 C. Bianchini, A. Meli, M. Peruzzini, P. Frediani, C. Bohanna, M. A. Esteruelas and L. A. Oro, *Organometallics*, 1992, **11**, 138–145.
14 E. J. Daida and J. C. Peters, *Inorg. Chem.*, 2004, **43**, 7474–7485.
15 R. J. Trovitch, E. Lobkovsky, E. Bill and P. J. Chirik, *Organometallics*, 2008, **27**, 1470–1478.

16 H. Fong, M.-E. Moret, Y. Lee and J. C. Peters, *Organometallics*, 2013, **32**, 3053–3062.
17 S. Chakraborty, W. W. Brennessel and W. D. Jones, *J. Am. Chem. Soc.*, 2014, **136**, 8564–8567.
18 S. Chakraborty, P. O. Lagaditis, M. Förster, E. A. Bielinski, N. Hazari, M. C. Holthausen, W. D. Jones and S. Schneider, *ACS Catal.*, 2014, **4**, 3994–4003.
19 C. Darcel and J. B. Sortais, Iron-Catalyzed Reduction and Hydroelementation Reactions, in *Iron Catalysis Ii*, ed. E. Bauer, Springer-Verlag Berlin, Berlin, 2015, vol. 50, pp. 173–216.
20 H. Dai and H. Guan, *Isr. J. Chem.*, 2017, **57**, 1170–1203.
21 W. H. Bernskoetter and N. Hazari, *Acc. Chem. Res.*, 2017, **50**, 1049–1058.
22 Y. Sunada, H. Ogushi, T. Yamamoto, S. Uto, M. Sawano, A. Tahara, H. Tanaka, Y. Shiota, K. Yoshizawa and H. Nagashima, *J. Am. Chem. Soc.*, 2018, **140**, 4119–4134.
23 S. C. Bart, E. Lobkovsky and P. J. Chirik, *J. Am. Chem. Soc.*, 2004, **126**, 13794–13807.
24 R. J. Trovitch, E. Lobkovsky and P. J. Chirik, *Inorg. Chem.*, 2006, **45**, 7252–7260.
25 R. P. Yu, J. M. Darmon, J. M. Hoyt, G. W. Margulieux, Z. R. Turner and P. J. Chirik, *ACS Catal.*, 2012, **2**, 1760–1764.
26 D. Srimani, Y. Diskin-Posner, Y. Ben-David and D. Milstein, *Angew. Chem., Int. Ed.*, 2013, **52**, 14131–14134.
27 R. Xu, S. Chakraborty, S. M. Bellows, H. Yuan, T. R. Cundari and W. D. Jones, *ACS Catal.*, 2016, **6**, 2127–2135.
28 J. C. Ott, C. K. Blasius, H. Wadepohl and L. H. Gade, *Inorg. Chem.*, 2018, **57**, 3183–3191.
29 L. J. Murphy, M. J. Ferguson, R. McDonald, M. D. Lumsden and L. Turculet, *Organometallics*, 2018, **37**, 4814–4826.
30 N. Gorgas, J. Brünig, B. Stöger, S. Vanicek, M. Tilset, L. F. Veiros and K. Kirchner, *J. Am. Chem. Soc.*, 2019, **141**, 17452–17458.
31 J. Zhang, M. Gandelman, D. Herrman, G. Leitus, L. J. W. Shimon, Y. Ben-David and D. Milstein, *Inorg. Chim. Acta*, 2006, **359**, 1955–1960.
32 D. Benito-Garagorri, L. G. Alves, M. Puchberger, K. Mereiter, L. F. Veiros, M. J. Calhorda, M. D. Carvalho, L. P. Ferreira, M. Godinho and K. Kirchner, *Organometallics*, 2009, **28**, 6902–6914.
33 B. Bichler, C. Holzhacker, B. Stöger, M. Puchberger, L. F. Veiros and K. Kirchner, *Organometallics*, 2013, **32**, 4114–4121.
34 I. Koehne, T. J. Schmeier, E. A. Bielinski, C. J. Pan, P. O. Lagaditis, W. H. Bernskoetter, M. K. Takase, C. Würtele, N. Hazari and S. Schneider, *Inorg. Chem.*, 2014, **53**, 2133–2143.
35 P. O. Lagaditis, P. E. Sues, J. F. Sonnenberg, K. Y. Wan, A. J. Lough and R. H. Morris, *J. Am. Chem. Soc.*, 2014, **136**, 1367–1380.
36 M. Glatz, N. Gorgas, B. Stöger, E. Pittenauer, L. Ferreira, L. F. Veiros, M. J. Calhorda and K. Kirchner, *Z. Anorg. Allg. Chem.*, 2021, **647**, 1429–1435.
37 F. Schneck, M. Assmann, M. Balmer, K. Harms and R. Langer, *Organometallics*, 2016, **35**, 1931–1943.
38 C. V. Thompson, H. D. Arman and Z. J. Tonzetich, *Organometallics*, 2017, **36**, 1795–1802.
39 S. Pal, *Organometallics*, 2023, **42**, 3099–3108.
40 D. K. Pandey, E. Khaskin, S. Pal, R. R. Fayzullin and J. R. Khusnutdinova, *ACS Catal.*, 2023, **13**, 375–381.
41 D. K. Pandey, E. Khaskin and J. R. Khusnutdinova, *ChemCatChem*, 2023, **15**, e202300644.
42 S. Sang, T. Unruh, S. Demeshko, L. I. Domenianni, N. P. van Leest, P. Marquetand, F. Schneck, C. Würtele, F. J. de Zwart, B. de Bruin, L. González, P. Vöhringer and S. Schneider, *Chem. – Eur. J.*, 2021, **27**, 16978–16989.
43 L. N. Mendelsohn, C. S. MacNeil, L. Tian, Y. Park, G. D. Scholes and P. J. Chirik, *ACS Catal.*, 2021, **11**, 1351–1360.
44 J. Derosa, P. Garrido-Barros and J. C. Peters, *J. Am. Chem. Soc.*, 2021, **143**, 9303–9307.
45 J. A. Widegren and R. G. Finke, *J. Mol. Catal. A: Chem.*, 2003, **198**, 317–341.
46 C. A. Jaska and I. Manners, *J. Am. Chem. Soc.*, 2004, **126**, 9776–9785.
47 J. F. Sonnenberg, N. Coombs, P. A. Dube and R. H. Morris, *J. Am. Chem. Soc.*, 2012, **134**, 5893–5899.
48 N. Gorgas, L. G. Alves, B. Stöger, A. M. Martins, L. F. Veiros and K. Kirchner, *J. Am. Chem. Soc.*, 2017, **139**, 8130–8133.
49 Y. Zhao and D. G. Truhlar, *J. Chem. Phys.*, 2006, **125**, 194101.
50 F. Weigend and R. Ahlrichs, *Phys. Chem. Chem. Phys.*, 2005, **7**, 3297–3305.
51 M. J. Frisch, G. W. Trucks, H. B. Schlegel, G. E. Scuseria, M. A. Robb, J. R. Cheeseman, G. Scalmani, V. Barone, G. A. Petersson, H. Nakatsuji, X. Li, M. Caricato, A. V. Marenich, J. Bloino, B. G. Janesko, R. Gomperts, B. Mennucci, H. P. Hratchian, J. V. Ortiz, A. F. Izmaylov, J. L. Sonnenberg, D. Williams-Young, F. Ding, F. Lipparini, F. Egidi, J. Goings, B. Peng, A. Petrone, T. Henderson, D. Ranasinghe, V. G. Zakrzewski, J. Gao, N. Rega, G. Zheng, W. Liang, M. Hada, M. Ehara, K. Toyota, R. Fukuda, J. Hasegawa, M. Ishida, T. Nakajima, Y. Honda, O. Kitao, H. Nakai, T. Vreven, K. Throssell, J. A. Montgomery Jr., J. E. Peralta, F. Ogliaro, M. J. Bearpark, J. J. Heyd, E. N. Brothers, K. N. Kudin, V. N. Staroverov, T. A. Keith, R. Kobayashi, J. Normand, K. Raghavachari, A. P. Rendell, J. C. Burant, S. S. Iyengar, J. Tomasi, M. Cossi, J. M. Millam, M. Klene, C. Adamo, R. Cammi, J. W. Ochterski, R. L. Martin, K. Morokuma, O. Farkas, J. B. Foresman and D. J. Fox, *Gaussian 16, Revision C.01*, Gaussian, Inc., Wallingford CT, 2019.
52 A. V. Marenich, C. J. Cramer and D. G. Truhlar, *J. Phys. Chem. B*, 2009, **113**, 6378–6396.
53 D. G. Gusev, *Organometallics*, 2013, **32**, 4239–4243.
54 (*a*) D. K. Pandey, T. Gridneva, E. Khaskin, R. R. Fayzullin, S. Vasylevskyi and J. R. Khusnutdinova, CCDC 2447918: Experimental Crystal Structure Determination, 2025, DOI: **10.5517/ccdc.csd.cc2n5837**; (*b*) D. K. Pandey, T. Gridneva, E. Khaskin, R. R. Fayzullin, S. Vasylevskyi and

J. R. Khusnutdinova, CCDC 2447919: Experimental Crystal Structure Determination, 2025, DOI: 10.5517/ccdc.csd.cc2n5848; (*c*) D. K. Pandey, T. Gridneva, E. Khaskin, R. R. Fayzullin, S. Vasylevskyi and J. R. Khusnutdinova, CCDC 2447920: Experimental Crystal Structure Determination, 2025, DOI: 10.5517/ccdc.csd.cc2n5859; (*d*) D. K. Pandey, T. Gridneva, E. Khaskin, R. R. Fayzullin, S. Vasylevskyi and J. R. Khusnutdinova, CCDC 2447921: Experimental Crystal Structure Determination, 2025, DOI: 10.5517/ccdc.csd.cc2n586b.